RESEARCH ARTICLE
SPACE PHYSICS

Earth and Planetary Physics
8: 797–810, 2024
doi: 10.26464/epp2024049

Solar energetic particles intensity variations associated with a tilted-dipole 3D corotating interaction region

YuJi Zhu[1,2,3], Fang Shen[1,3*], Xi Luo[2], Yang Wang[4], and BoFeng Tang[1]

[1]State Key Laboratory of Space Weather, National Space Science Center, Chinese Academy of Sciences, Beijing 100190, China;

[2]Shandong Institute of Advanced Technology (SDIAT), Jinan 250100, China;

[3]College of Earth and Planetary Sciences, University of Chinese Academy of Sciences, Beijing 100049, China;

[4]School of Science, Harbin Institute of Technology, Shenzhen 518055, China

Key Points:

- The focusing effect can result in a rippled peak intensity distribution of energetic particles in corotating interaction regions.
- The observed discrepancies in the radial variation of the particle peak intensity can be attributed to the structure of the solar wind.
- Spectral indices at different radial distances may be close in corotating interaction regions.

Citation: Zhu, Y. J., Shen, F., Luo, X., Wang, Y., and Tang, B. F. (2024). Solar energetic particles intensity variations associated with a tilted-dipole 3D corotating interaction region. *Earth Planet. Phys.*, *8*(5), 797–810. http://doi.org/10.26464/epp2024049

Abstract: The effect of a tilted-dipole three-dimensional corotating interaction region (CIR) on the transport and acceleration of solar energetic particles (SEPs) is studied. In this work, we discussed how the particle intensity longitudinal and radial dependence might be influenced by the background structures. Moreover, we investigate how the spectral index distribution is modulated by the CIR structure. We use the focused transport equation (FTE) to describe the propagation and acceleration of SEPs in a tilt-dipole 3D CIR, generated by the high-resolution 3D magnetohydrodynamic (MHD) model. The forward stochastic differential method is used to solve the FTE. The protons with the $E^{-4.4}$ spectrum from 0.5 to 15 MeV are injected uniformly at the heliographic equator of 0.15 AU. Physical quantities are extracted along each interplanetary magnetic field (IMF) line to show the results. In the tilted-dipole CIR background, if injected from the solar equator at the inner boundary, particles in the slow flow are transported to higher latitudes due to the extension of the IMF lines to higher latitudes. The longitudinal patterns of the particles are dominated by the density of IMF lines. The focusing effect modulates the longitudinal variation of the particle intensity and gives rise to new longitudinal intensity peaks. The adiabatic effect largely increases the intensity fluctuation along the longitude. The structure of the solar wind can also lead to the difference of the index α in the empirical function $I_{max} = kR^{-\alpha}$, describing the radial variation of peak intensity according to our simulation. Under the influence of the CIR structure, the index α varies from 1.9 to 3.4 at 0.3–1.0 AU. The variation of the solar wind speed should be considered when estimating the radial dependence of the SEP peak intensity. The spectra indices rise near the CIR boundaries and drop near the stream interface (SI). The adiabatic effect makes the spatial variability of the spectral index larger. The spectral index could be similar at different radial distances in the CIR structure.

Keywords: solar energetic particle (SEP); corotating interaction regions (CIR); magnetohydrodynamic (MHD)

1. Introduction

During solar eruptions, sudden strong enhancement of the flux of high energy particles from about 10 keV to a few GeV is occasionally observed by particle monitors. These events are called Solar Energetic Particle (SEP) events (Reames, 1999; Desai and Giacalone, 2016). Since SEPs affect not only technology but also human health in modern society, it is important to study the propagation and acceleration of SEPs. With the development of interplanetary travel, it is necessary to predict the potential impact of SEPs on space crafts. Therefore, the spatial distribution and the time evolution of SEPs has aroused interest from more and more researchers.

The spatial variation of energetic particles has been studied by multi-spacecraft measurements of SEP events. The longitudinal distributions of the peak intensities in the impulsive events could be approximated by Gaussian functions near 1 AU (Lario et al., 2013; Richardson et al., 2014). Some research found that the longitudinal distributions are generally asymmetric (He HQ and Wan W, 2017). The longitudinal distribution is also suggested to be Gaussian distributions superposed with narrow peaks (fingers), but the origin is not clear yet (Klassen et al., 2016). The radial dependency of peak intensities $I(R)$ is usually described by the functional form $I_{max} = kR^{-\alpha}$, where R is the radial distance. The index $-\alpha$ varied in a

First author: Y. J. Zhu, yjzhu@spaceweather.ac.cn
Correspondence to: F. Shen, fshen@spaceweather.ac.cn
Received 02 APR 2024; Accepted 23 AUG 2024.
First Published online 04 SEP 2024.

wide range in the observations. It was found to be in a range of −5.5 to 4.5, with a median value of −2 for 4–13 MeV protons (Kallenrode, 1997). Lario et al. (2006) found the index $-\alpha$ varying from −2.7 (considering the absolute maximum intensities) to −2.1 (considering only maximum intensities without local enhancements) for 4–13 MeV protons.

Numerical simulations have also been performed to understand the physical processes underlying the spatial distribution. According to the numerical studies (He HQ and Wan W, 2015; Strauss and Fichtner, 2015), which included perpendicular diffusion into a numerical SEP transport model, the longitudinal asymmetry is attributed to the asymmetry topology of the magnetic field and the effects of perpendicular diffusion. Lario et al. (2007) solved the focused-diffusion transport equation in the background described by an Archimedean spiral magnetic field. They concluded that the particle energy, the mean free path, and the duration of the particle injection all contribute to the radial distribution. He HQ and Wan W (2017) solved the five-dimensional Fokker–Planck transport equation in a three-dimensional Parker field. They suggested that the index $-\alpha$ in the function $I_{\max} = kR^{-\alpha}$ mainly depends on the separations between the sources and the magnetic field line foot point of the observers.

In addition, the effect of large-scale solar wind structures has received more and more attention. The Corotation interaction region (CIR) is a typical large-scale structure in the interplanetary space, formed when fast solar wind catches slow solar wind (Smith and Wolfe, 1979). This configuration was found (Neugebauer, 1962) and has been confirmed with numerous observations (Richardson, 2004). In the earlier numerical studies, it is found that the corotating solar wind structures could accelerate SEPs effectively and modify the SEP intensity, energy spectra and anisotropy (Kocharov, 2003; Kocharov et al., 2008, Tsubouchi, 2014). Recently, three-dimensional Magnetohydrodynamic (MHD) simulations were used to describe the background fields with complex interplanetary stream structures (Kocharov et al., 2009; Kozarev et al., 2010). Wei WW et al. (2019) coupled the SEP with realistic solar wind background and concluded that the multiple flux peaks in the profiles are mainly caused by the magnetic focusing effect. Wijsen et al. (2019b) coupled the SEP with a CIR background and found that the intensity varies strongly along selected IMF lines and the longitudinal intensity is highly asymmetric near the CIR.

More work is needed to understand how the solar wind background affects the spatial variation of energetic particles during propagation. The Parker field is the most commonly used background for the solar wind in previous studies. The particle spatial variation is usually attributed to the interplanetary diffusion or seed populations (Lario et al., 2007; He HQ and Wan W, 2015; Strauss and Fichtner, 2015; He HQ and Wan W, 2017). The effect of the background construction on the spatial variation of energetic particles requires further analysis with a 3D numerical background. In this work, we construct a dipole-tilted CIR with a three-dimensional Magnetohydrodynamic (MHD) model and then couple it to a particle transport model. In the 3D MHD model, given the boundary conditions, the background physical quantities, such as solar wind velocity, magnetic field, etc., could be obtained by solving the MHD equations with Corona-interplanetary Total Variation Diminishing (COIN-TVD) model (Feng XS et al., 2003; 2007, Shen F et al., 2009). The particle transport model describes particle propagation by solving the focused transport equation (FTE) (Skilling, 1971; Isenberg, 1997; le Roux and Webb, 2009; Zhang M et al., 2009) with a time-forward Markov stochastic method (Kopp et al., 2012; Bobik et al., 2016; Strauss and Effenberger, 2017). The background parameters in the FTE are provided by the MHD model. We then use this model to investigate the effect of large-scale background on particle intensity variability in flare-only events (since the coronal mass ejections (CMEs) are not included in the model).

The article is structured as follows. In Section 2, we introduce the equations in our model and the numerical details. In Section 3 we present the CIR background condition and discuss the CIR background effect on the SEP variation with longitude, the radial dependence of proton peak intensities and the SEP spectra variation. A summary is given in Section 4.

2. Methods

2.1 MHD Model

The background is obtained by solving the ideal magnetohydrodynamic (MHD) equations with total variation diminishing Lax–Friedrichs (TVD/LF) scheme (Feng XS et al., 2003; 2007, Shen F et al., 2009). The MHD equations are as followed:

$$\frac{\partial \rho}{\partial t} + \nabla \cdot (\rho \boldsymbol{U}) = 0, \tag{1}$$

$$\frac{\partial (\rho \boldsymbol{U})}{\partial t} + \nabla \cdot \left[\left(P + \frac{B^2}{2\mu_0} \right) \boldsymbol{I} + \rho \boldsymbol{U}\boldsymbol{U} - \frac{\boldsymbol{B}\boldsymbol{B}}{\mu_0} \right] = -\frac{\rho G M_s}{r^3} \boldsymbol{r} + \boldsymbol{U} \cdot \boldsymbol{f}, \tag{2}$$

$$\frac{\partial \boldsymbol{B}}{\partial t} + \nabla \cdot (\boldsymbol{U}\boldsymbol{B} - \boldsymbol{B}\boldsymbol{U}) = 0, \tag{3}$$

$$\frac{\partial \boldsymbol{P}}{\partial t} + \nabla \cdot (\boldsymbol{P}\boldsymbol{U}) = -(\gamma - 1)\boldsymbol{P} \nabla \cdot \boldsymbol{U}, \tag{4}$$

where ρ is the mass density, $\boldsymbol{U}$ is the solar wind velocity, $\boldsymbol{I}$ is the unit tensor, $\boldsymbol{B}$ is the magnetic field vector, $\boldsymbol{r}$ is the radial vector, $\boldsymbol{P}$ is the thermal pressure, and γ is the polytrophic index. The empirical γ was derived to be 1.46 (Totten et al., 1995). $\boldsymbol{f}$ is the additional fictitious force density introduced into the momentum equation as a consequence of the coordinate transformation. We use geometric meshes in the radial direction ranging from $0.35R_s$ to $6.19R_s$ (R_s is the solar radius), with solution region from 0.1 to 10.0 AU. A six-piece grid system (Feng XS et al., 2010) was adopted on the spherical surface with a spatial resolution of 1° × 1°.

We choose the potential field source surface (PFSS) model to describe the corona magnetic field (Altschuler and Newkirk, 1969; Schatten et al., 1969). The polarity of interplanetary magnetic field can be predicted very well by the PFSS model. Subsequent magnetic field models are improved on this basis. In the PFSS model, we assume that there are no currents above the photosphere, therefore $\nabla \times \boldsymbol{B} = 0$. The magnetic field can be written as $\boldsymbol{B} = -\nabla\psi$. Since $\nabla \cdot \boldsymbol{B} = 0$, we can obtain the Laplace equation $\nabla^2\psi = 0$. The solution in the spherical coordinates for the domain $r \geq R_s$ (R_s is the solar radius) is

$$\psi(r,\theta,\phi) = R_s \sum_{n=1}^{\infty}\sum_{m=0}^{n}[(\frac{R_s}{r})^{n+1}(g_n^m \cos m\phi + h_n^m \sin m\phi)P_n^m(\theta)], \quad (5)$$

where $P_n^m(\theta)$ is Legendre Polynomials, g_n^m and h_n^m are harmonic coefficients. g_1, h_1 are dipole terms. g_1^0 is the axial dipole term and g_1^1, h_1^1 are equatorial dipole terms. We choose different harmonic coefficients to construct the coronal magnetic field. In this work, in order to obtain a dipole field with a tilt angle between solar rotation axis and dipole axis of about 35 degrees, we set $g_1^0 : g_1^1 = 2 : 1$ and $h_1^1 = g_1^1$ ($h_l^m = 0$ and $g_l^m = 0$ when $l > 1$).

The inner boundary is set at 0.1 AU. The inner boundary conditions are given by empirical formulae (Shen F et al., 2018). We use a simplified WSA coronal solar wind model (Arge et al., 2003) to set the radial velocity at the inner boundary (as shown in the left panel of Figure 1):

$$U_r = U_s + \frac{U_f}{(1+f_s)^{a_1}}\left[1 - 0.8\exp\left(-\frac{\theta_b}{a_2}\right)\right], \quad (6)$$

where f_s is the corona magnetic field expansion factor, θ_b is the minimum angular distance that an open field foot point lies from a coronal hole boundary. We calculate f_s and θ_b from the coronal magnetic field. a_1 adjusts the effect of f_s and a_2 determines the width of the low speed flow. U_s is the minimum possible speed and U_f determines the maximum speed. We set $a_1 = \frac{2}{9}$, $a_2 = 2$, $U_s = 294$ km s^{-1} and $U_f = 387$ km s^{-1} in this work.

The radial magnetic field is assumed to be uniform at the inner boundary. The influence of the current sheet on particles is not included in this work.

Then the radial magnetic field is

$$B_r = |\frac{1}{\sqrt{2}}\text{mean}(B_0)(1/R_b)^2|, \quad (7)$$

where mean(B_0) is the average value of the observed magnetic field at 1 AU. We set $\frac{1}{\sqrt{2}}\text{mean}(B_0) = 4.0$ nT in this work. The temperature is

$$T_p = \frac{1}{2}U_r^2 \times (1/R_b)^{2(\gamma-1)}, \quad (8)$$

where $\gamma = 1.46$ is the polytrophic index. $R_b = 0.1$ (the unit is AU) is the inner boundary radius. The number density is

$$N = N_0(1/R_b)^2 U_0(\frac{1}{2}U_0^2 + \frac{GM_s}{R_s}) \times [(U_r+50)(\frac{1}{2}(U_r+50)^2 + \frac{GM_s}{R_s})]^{-1}, \quad (9)$$

where $U_0 = 750$ km s^{-1}, G is the gravitational constant, M_s is the solar mass, R_s is the solar radius (Feng et al., 2010). We set $N_0 = 2.0$ cm^{-3}. The latitudinal and longitudinal solar wind speeds are

$$U_\theta = 0,\ U_\phi = -WR_b\sin(\theta), \quad (10)$$

where W is the solar rotation rate, R_b is the radial distance of inner boundary. The latitudinal and longitudinal magnetic fields are set as

$$B_\theta = 0,\ B_\phi = B_r\frac{U_\phi}{U_r}. \quad (11)$$

The right panel in Figure 1 shows the snapshot of the radial solar wind speed in the equatorial and meridional plane simulated with our model. The magnetic field lines superposed are all with foot-points on the solar equator. As shown in Figure 1, the magnetic field lines are compressed in the longitudinal direction and stretch northward and southward.

Since the magnetic field lines vary in latitude and longitude with the radial distance, we examine the distribution along each magnetic field line to present the results more clearly. We extract the information of background and particles from each magnetic line and mark each magnetic line with its foot point longitude φ_{fp} (All the magnetic field lines we study are derived from the equatorial plane at 0.1 AU).

Figure 2 shows the physical quantities of the background extracted along each magnetic field line as a function of heliocentric radial distance. The left panel shows the reciprocal of focusing length L_B^{-1} (see Section 2.2 in detail). The right panel shows the divergence of the solar wind speed ($\nabla \cdot \boldsymbol{U}$). Their pattern is similar because of the assumption of the frozen-in field effect ($L_B^{-1} = -\boldsymbol{b}\cdot\nabla \ln B = \nabla\cdot\boldsymbol{b}$ since $\nabla\cdot\boldsymbol{B} = 0$). The negative values in the graph are the locations of the compression regions. A negative

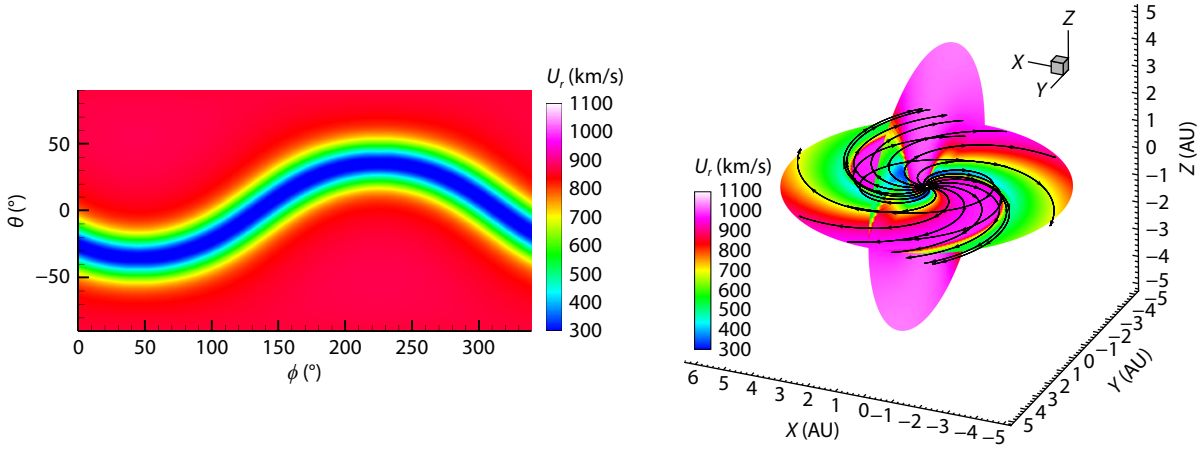

Figure 1. The left panel shows the inner boundary conditions of radial solar wind speed U_r (km/s) used in this article. The right panel shows U_r in the heliospheric equatorial and meridional plane (from 0.1 AU to 5.0 AU) in this model, superposed with magnetic field lines.

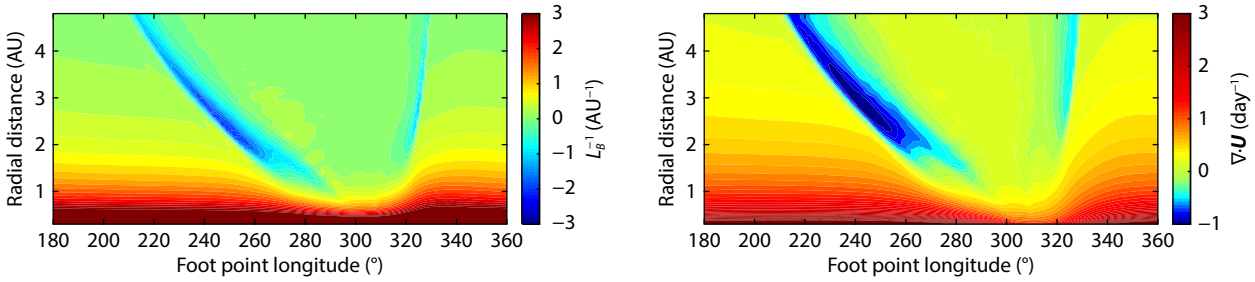

Figure 2. The left panel shows the reciprocal of focusing length L_B^{-1} and the right panel shows the divergence of the solar wind speed.

value of $\nabla \cdot \boldsymbol{U}$ indicates that the particles can be accelerated adiabatically, whereas a negative L_B^{-1} value suggests that the particles tend to be reflected back to the smaller radial distances.

We define the stream interface (SI) as where the solar wind speed (and the temperature) increases, the magnetic field (and the number density) is compressed, and the total perpendicular pressure (the sum of magnetic pressure and plasma thermal pressure perpendicular to the magnetic field) peaks (Jian L et al., 2006). The boundaries are where the pressure emerges from and decays back to the background (Jian L et al., 2006). If the solar wind speed increases, accompanied by simultaneous enhancements in density and temperature, then the disturbance is a forward compression; whereas the solar wind speed increases with decreasing density and temperature in a reverse compression. The corresponding structures of the magnetic field strength, the reciprocal of the focusing length, the solar wind speed, etc., are illustrated in the Fig. 1 of Kocharov et al. (2003).

2.2 SEP Model

We describe the particles with the phase-space distribution function $f(\boldsymbol{x}, p, \mu, t)$. We solve FTE to model its evolution.

The full FTE for the particle distribution function can be written as (without the stochastic diffusion D_{pp}, cross-field diffusion $\kappa_\perp$ and the drift velocity $\boldsymbol{V}_d$) (Skilling, 1971; Isenberg, 1997; le Roux and Webb, 2009; Zhang M et al., 2009):

$$\frac{\partial f}{\partial t} = \frac{\partial}{\partial \mu} D_{\mu\mu} \frac{\partial f}{\partial \mu} - \frac{\mathrm{d}\boldsymbol{X}}{\mathrm{d}t} \cdot \nabla f - \frac{\mathrm{d}\mu}{\mathrm{d}t} \frac{\partial f}{\partial \mu} - \frac{\mathrm{d}p}{\mathrm{d}t} \frac{\partial f}{\partial p} + S, \tag{12}$$

where,

$$\frac{\mathrm{d}\boldsymbol{X}}{\mathrm{d}t} = \boldsymbol{U} + v\mu\boldsymbol{b}, \tag{13}$$

$$\frac{\mathrm{d}p}{\mathrm{d}t} = -\left[\frac{1-\mu^2}{2}(\nabla \cdot \boldsymbol{U} - \boldsymbol{bb} : \nabla \boldsymbol{U}) + \mu^2 \boldsymbol{bb} : \nabla \boldsymbol{U}\right] p - \frac{\mu p}{v} \frac{\mathrm{d}\boldsymbol{U}}{\mathrm{d}t} \cdot \boldsymbol{b}, \tag{14}$$

$$\frac{\mathrm{d}\mu}{\mathrm{d}t} = \frac{(1-\mu^2)v}{2L_B} + \frac{\mu(1-\mu^2)}{2}(\nabla \cdot \boldsymbol{U} - 3\boldsymbol{bb} : \nabla \boldsymbol{U}) - \frac{1-\mu^2}{v} \frac{\mathrm{d}\boldsymbol{U}}{\mathrm{d}t} \cdot \boldsymbol{b}, \tag{15}$$

where $L_B^{-1} = -\boldsymbol{b} \cdot \nabla \ln B$. $\boldsymbol{X}$, p and μ are the particle spatial location, momentum and cosine of pitch-angle respectively. v is the particle speed. $D_{\mu\mu}$ is the pitch-angle diffusion coefficient. $\boldsymbol{b}$ is the unit vector of magnetic field. $\boldsymbol{U}$ is the solar wind velocity. The terms on the right-hand side of Equation (12) describe the process of pitch-angle diffusion, changes in spatial location, changes in pitch angle, changes in momentum magnitude, and the source of the particles, respectively.

$$D_{\mu\mu} = D_0 v p^{-2/3} (1-\mu^2)\{|\mu|^{q-1} + h\} k(x), \tag{16}$$

where $k(x) = (B_r/B)^2$, and $q > 1$ is the slope of the power spectrum. The constant h is introduced to help particles transport through $\mu = 0$ in simulation. We set $h = 0.05$, $q = 5/3$.

The parallel mean free path is related to $D_{\mu\mu}$ through:

$$\lambda_{//} = \frac{3v}{8} \int_{-1}^{+1} \frac{(1-\mu^2)^2}{D_{\mu\mu}} \mathrm{d}\mu. \tag{17}$$

Similar to Dröge et al. (2010) and Wijsen et al. (2019b), we set constant radial mean free path $\lambda_r^{//} = 0.3$ AU for 4 MeV particles. We consider neither the cross-field diffusion $\kappa_\perp$ nor the drift velocity $\boldsymbol{V}_d$ in our model.

Equation (12) can be written as follows:

$$\begin{aligned} \frac{\partial f}{\partial t} = {} & \frac{\partial^2}{\partial \mu^2}(D_{\mu\mu} f) - \nabla \cdot \left(\frac{\mathrm{d}\boldsymbol{X}}{\mathrm{d}t} f\right) - \frac{\partial}{\partial \mu}\left[\left(\frac{\partial D_{\mu\mu}}{\partial \mu} + \frac{\mathrm{d}\mu}{\mathrm{d}t}\right) f\right] \\ & - \frac{\partial}{\partial p}\left(\frac{\mathrm{d}p}{\mathrm{d}t} f\right) + \left[\nabla \cdot \frac{\mathrm{d}\boldsymbol{X}}{\mathrm{d}t} + \frac{\partial}{\partial \mu}\left(\frac{\mathrm{d}\mu}{\mathrm{d}t}\right) + \frac{\partial}{\partial p}\left(\frac{\mathrm{d}p}{\mathrm{d}t}\right)\right] f + S. \end{aligned} \tag{18}$$

Since

$$\begin{aligned} & \nabla \cdot \frac{\mathrm{d}\boldsymbol{X}}{\mathrm{d}t} + \frac{\partial}{\partial \mu}\left(\frac{\mathrm{d}\mu}{\mathrm{d}t}\right) + \frac{\partial}{\partial p}\left(\frac{\mathrm{d}p}{\mathrm{d}t}\right) \\ & \quad = (1-\mu^2)\nabla \cdot \boldsymbol{U} + (3\mu^2 - 1)\boldsymbol{bb} : \nabla \boldsymbol{U} + \frac{\mu}{v} \frac{\mathrm{d}\boldsymbol{U}}{\mathrm{d}t} \cdot \boldsymbol{b} \\ & \quad = -\frac{2}{p} \frac{\mathrm{d}p}{\mathrm{d}t} - \frac{\mu}{v} \frac{\mathrm{d}\boldsymbol{U}}{\mathrm{d}t} \cdot \boldsymbol{b}, \end{aligned} \tag{19}$$

the Equation (18) can be written as:

$$\begin{aligned} \frac{\partial f}{\partial t} = {} & \frac{\partial^2}{\partial \mu^2}(D_{\mu\mu} f) - \nabla \cdot \left(\frac{\mathrm{d}\boldsymbol{X}}{\mathrm{d}t} f\right) \\ & - \frac{\partial}{\partial \mu}\left[\left(\frac{\partial D_{\mu\mu}}{\partial \mu} + \frac{\mathrm{d}\mu}{\mathrm{d}t}\right) f\right] - \frac{\partial}{\partial p}\left(\frac{\mathrm{d}p}{\mathrm{d}t} f\right) - L_F f + S, \end{aligned} \tag{20}$$

where $L_F = \frac{2}{p} \frac{\mathrm{d}p}{\mathrm{d}t} + \frac{\mu}{v} \frac{\mathrm{d}\boldsymbol{U}}{\mathrm{d}t} \cdot \boldsymbol{b}$ is the loss term.

Note that the form of the Equation (20) is not "completely" conservative. The remaining terms that cannot be included in the conservative terms are included in the linear loss term L_F. We treat these terms as linear losses in the transport processes. We then solve the FTE by the time-forward stochastic difference equation (SDE) (Kopp et al., 2012; Bobik et al., 2016; Strauss and Effenberger, 2017).

The corresponding forward SDEs are

$$\begin{cases} \mathrm{d}\boldsymbol{X} = \dfrac{\mathrm{d}\boldsymbol{X}}{\mathrm{d}t}\mathrm{d}t, \\ \mathrm{d}p = \dfrac{\mathrm{d}p}{\mathrm{d}t}\mathrm{d}t, \\ \mathrm{d}\mu = \left(\dfrac{\partial D_{\mu\mu}}{\partial \mu} + \dfrac{\mathrm{d}\mu}{\mathrm{d}t}\right)\mathrm{d}t + \sqrt{2D_{\mu\mu}}\mathrm{d}w_{\mu}, \end{cases} \tag{21}$$

where $\mathrm{d}w_{\mu}$ describes the Wiener process. In the forward case, there are two methods to release the pseudo-particles (Kopp et al., 2012; Bobik et al., 2016). In the first method, the initial weight of each pseudo-particle is set to $\alpha_i = 1$. The initial position and time are determined by the rejection sampling from source or boundary distribution function $S(q, t)$ (normalized to unity). The second method generates the initial positions and time according to a specific distribution. The initial weights are set to $\alpha_i = S(q, t)g^{-1}$, where g is the generated distribution. For a uniform distribution, $g = 1$. We use the second way to release the pseudo-particles.

With the loss term L_F, the weight α_i changes along the trajectory following

$$\alpha_i(nt) = \alpha_i(nt-1)\mathrm{e}^{-L_F(nt)\mathrm{d}t}, \tag{22}$$

where $\mathrm{d}t$ is the time step and nt is the number of time step. If $\mathrm{d}t$ doesn't change, we have

$$\alpha_i(nt) = \alpha_i(nt-1)\mathrm{e}^{-L_F(nt)\mathrm{d}t} = \alpha_i(t=0)\mathrm{e}^{-\sum_{k=1}^{nt}(L_{F,k}\mathrm{d}t)}. \tag{23}$$

To obtain the results, we apply a binning procedure (Kopp et al., 2012). Note that the FTE is written in the mixed coordinate (the spatial coordinate is measured in the stationary frame while the momentum and pitch angle are in the solar wind co-moving frame), so does our binning procedure. We record the weight α_i passing through each of the bins, which can be defined in our cases as

$$\begin{aligned} B^{(k,l,m,n,o)} = &\left[x_k - \frac{\Delta_{\mathrm{bin}}x}{2}, x_k + \frac{\Delta_{\mathrm{bin}}x}{2}\right] \times \left[y_l - \frac{\Delta_{\mathrm{bin}}y}{2}, y_l + \frac{\Delta_{\mathrm{bin}}y}{2}\right] \\ &\times \left[z_h - \frac{\Delta_{\mathrm{bin}}z}{2}, z_h + \frac{\Delta_{\mathrm{bin}}z}{2}\right] \times \left[p_m - \frac{\Delta_{\mathrm{bin}}p}{2}, p_m + \frac{\Delta_{\mathrm{bin}}p}{2}\right] \\ &\times \left[\mu_n - \frac{\Delta_{\mathrm{bin}}\mu}{2}, \mu_n + \frac{\Delta_{\mathrm{bin}}\mu}{2}\right] \times \left[t_o - \frac{\Delta_{\mathrm{bin}}t}{2}, t_o + \frac{\Delta_{\mathrm{bin}}t}{2}\right]. \end{aligned} \tag{24}$$

Because the time step $\mathrm{d}t$ may change with time and the result should not depend on $\mathrm{d}t$, for the same particle, we only calculate once during the time period $\left[t_o - \frac{\Delta_{\mathrm{bin}}t}{2}, t_o + \frac{\Delta_{\mathrm{bin}}t}{2}\right]$. We make sure $\Delta_{\mathrm{bin}}t$ is larger than every $\mathrm{d}t$ and is not too large. The same pseudo-particle may be counted several times in the same phase space bin later. To increase the statistics, we average over a time period δt. We choose $\delta t = M\Delta_{\mathrm{bin}}t, M \in N$.

In the time-forward case, we follow the steps: Firstly, release the pseudo-particles uniformly in the source areas. Set weight $\alpha_i = S(x_i, y_i, z_i, p_i, \mu_i, t_i)$. Secondly, the trajectories of pseudo-particles follow the forward SDEs (21). Weight α_i changes along the path following $\alpha_i(nt) = \alpha_i(nt-1)\mathrm{e}^{-L_F(nt)\mathrm{d}t}$. Thirdly, for each bin defined in Equation (24), we record the weights α_i of all the pseudo-particles passing. Fourthly, we normalize the results to ensure that the results do not change as the numbers of pseudo-particles released (the sizes of the injection intervals) and the sizes of bins change. The normalized result in each bin can be expressed as

$$\begin{aligned} &f(x_k, y_l, z_h, p_m, \mu_n, t_o) = \\ &\sum_{i=1}^{N} \alpha_i(k, l, h, m, n, o)\frac{\Delta_{\mathrm{inj}}x\Delta_{\mathrm{inj}}y\Delta_{\mathrm{inj}}z\Delta_{\mathrm{inj}}p\Delta_{\mathrm{inj}}\mu\Delta_{\mathrm{inj}}t}{\Delta_{\mathrm{bin}}x\Delta_{\mathrm{bin}}y\Delta_{\mathrm{bin}}z\Delta_{\mathrm{bin}}p\Delta_{\mathrm{bin}}\mu}, \end{aligned} \tag{25}$$

where Δ_{inj} is the injection interval. Finally, we average the results over a time period $\delta t = M\Delta_{\mathrm{bin}}t, M \in N$

$$< f(x, y, z, p, \mu, t) >= \frac{1}{M}\sum_{o} f(x_k, y_l, z_h, p_m, \mu_n, t_o). \tag{26}$$

We then obtain the particle differential intensity (per unit of kinetic energy) by

$$j_E = p^2 f_0(x, y, z, p, t), \tag{27}$$

where

$$f_0 = \frac{1}{2}\int_{-1}^{1} f(x, y, z, p, \mu, t)\mathrm{d}\mu. \tag{28}$$

The anisotropy is calculated by

$$A = 3\int_{-1}^{1} \mu f(x, y, z, p, \mu, t)\mathrm{d}\mu \Big/ \int_{-1}^{1} f(x, y, z, p, \mu, t)\mathrm{d}\mu. \tag{29}$$

The validation of our code is included in Appendix A.

3. Results and Discussion

We uniformly and isotropicly inject the protons from 0.5 to 15 MeV at the heliographic equator of 0.15 AU. The injection time profile is assumed to be (Reid, 1964)

$$f_b(t) = Q_0\frac{1}{t}\exp\left\{-\frac{\tau_c}{t} - \frac{t}{\tau_l}\right\}, \tag{30}$$

where τ_c and τ_l are the rise and decay timescales of the injection time profile, respectively. Q_0 is the normalization constant. We fit the profile after the event Parker Solar Probe (PSP) observed at 0.17 AU on DOY 094 of 2019 (see Leske et al., 2020). The τ_c is assumed to be 0.21 days and the τ_l is assumed to be 0.08 days (Zhao LL et al., 2020). The spectral index for the power-law fits is assumed to be –4.4. We use arbitrary units for the particle intensity because the specific value of the particle intensity does not affect our results in this work. The particles are uniformly injected at the inner boundary. We propagate particles with and without adiabatic cooling to investigate the effect of acceleration and transport on particle distribution. In the cases without adiabatic cooling, Equation (14) is not included (i.e., $\frac{\mathrm{d}p}{\mathrm{d}t} = 0$) in the simulation. The radial mean free path is constant ($\lambda_r = 0.3$ AU for 4 MeV protons), and the cross-field diffusion is not included. Since neither cross-field diffusion nor velocity drift is included, particles move along a single magnetic field line.

3.1 CIR Effect on SEP Variation with Longitude

3.1.1 The intensity of energetic particles

Figure 3 shows the particle intensity of corotating points varying with time at 1 AU. In the rising phase, the intensity increases at a similar rate. The peak intensity in the CIR (the green, yellow, and purple lines) is higher than that outside the CIR (the dark blue, light blue, and red lines). Moreover, the intensity inside the CIR

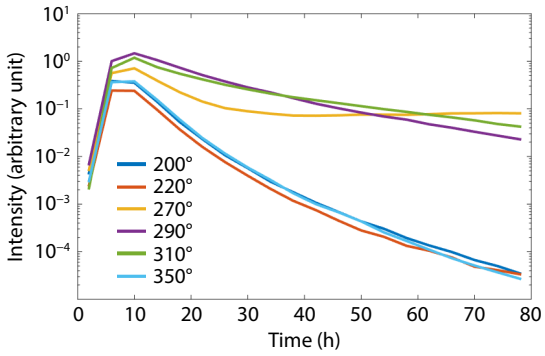

Figure 3. The intensity-time profile for 1–10 MeV protons at 1 AU. The lines with different colors represent the points at different IMF lines. The legend labels are the foot-point longitudes of the IMF lines.

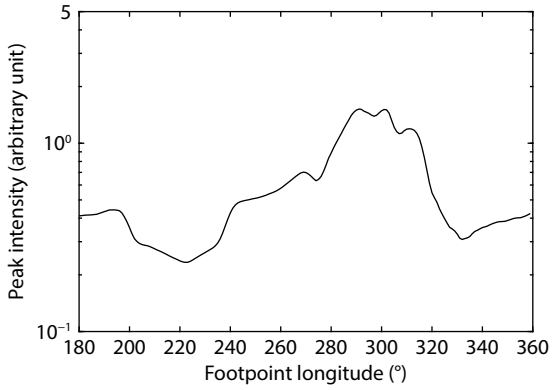

Figure 4. The peak intensity of 1–10 MeV protons varying with longitude at 1 AU.

decreases more slowly. Specifically, the intensity in the IMF line with $\varphi_{fp} \approx 270°$ decreases and then increases due to the acceleration by the reverse compression wave.

Figure 4 shows the particle peak intensity varying with the longitude at 1 AU. As we can see, several longitudinal peaks appear on account of this solar wind structure. This result provides an explanation for the concept of a rippled peak intensity distribution suggested by Klassen et al. (2016). Klassen et al. (2016) suggested a scenario of a Gaussian intensity distribution with narrow peaks (fingers). They proposed that this is due to the extension of open magnetic lines from the flare region into the interplanetary medium. Our results suggest that solar wind structures may also be responsible for this pattern. The peak intensity distribution does not show systemic east–west asymmetry due to the background structure, as discussed by He HQ and Wan W (2017). The effect of the cross-field diffusion is not considered in our study. The strong cross-field diffusion effect, which is not considered in our study, may smear the variation. Nevertheless, we provide a possible explanation for the variation in the observation.

Figure 5 shows the simulated solar wind speed, the number density, the temperature, the magnetic field magnitude, and the reciprocal of focusing length as a function of footpoint longitude, together with the corresponding 1–10 MeV proton intensity and anisotropy (in the descent phase of profiles in Figure 3). The physi-

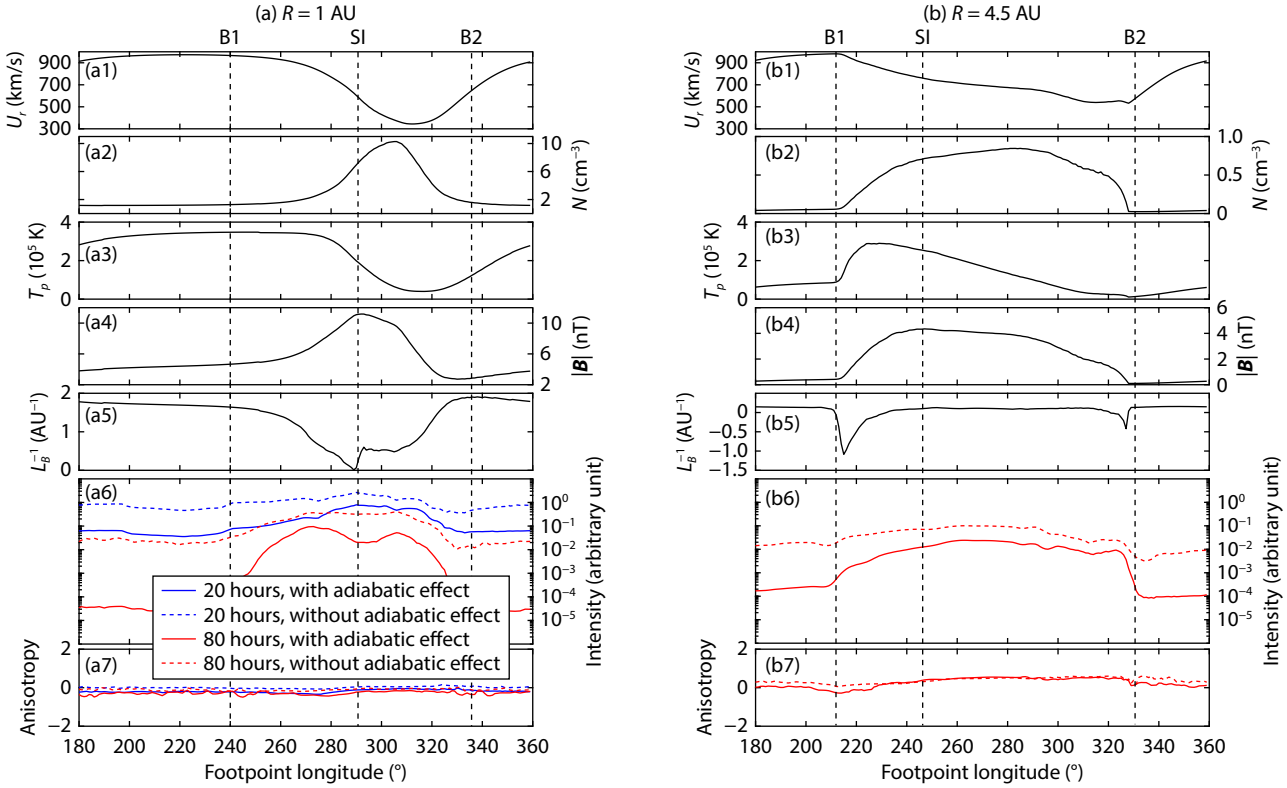

Figure 5. The radial solar wind speed (U_r), the number density (N), the temperature (T_p), the magnetic field intensity ($|\boldsymbol{B}|$), the reciprocal of focusing length (L_B^{-1}), the particle intensity, and the anisotropy distribution at 1 AU (a) and 4.5 AU (b). In Panel (a6–7) and (b6–7), the blue and red lines represent the results at 20 and 80 hours. The solid and dotted lines show the cases with and without the adiabatic effect.

cal quantities in the background are the results when the MHD simulation reaches a steady state. The left and right columns show these quantities at heliocentric radial distances of 1.0 AU and 4.5 AU, respectively. The vertical dashed lines indicate the boundaries (B1 and B2) and stream interface (SI) of the CIR. The method to define the boundaries and SI is described in Section 2.1.

At 1.0 AU (Panel (a6–7) in Figure 5), for the case without adiabatic cooling (the dotted lines), the variety of proton intensity at 20 and 80 hours along the longitude is consistent with that of the magnetic field magnitude. Since particles are uniformly injected at the inner boundary and move along the IMF lines, the particle intensity increases where the magnetic field lines are compressed. For the case with adiabatic cooling (the solid lines), the shape of the intensity profile is similar to that without adiabatic cooling but the variety becomes larger at 80 hours. An obvious dip forms near SI ($\varphi_{fp} \approx 290°$) at 80 hours due to the spatial distribution of the adiabatic cooling effect (the pattern of $\nabla \cdot \boldsymbol{U}$ is shown in the right panel of Figure 2). The particles in the left IMF lines ($\varphi_{fp} < 290°$) could be accelerated in the compressed region at larger radial distances. The particles in the right ($\varphi_{fp} > 290°$) experience less adiabatic cooling effect within 1.0 AU. In this way, a dip is formed near SI. Wijsen et al. (2019b) also found a decrease in the SI inside the CIR in their simulation. They explained that the IMF lines at the SI do not intersect the compression or shock waves that bound the CIR. The particles without the adiabatic cooling effect are nearly isotropic at 1.0 AU. Our results show that the formation of the dip is not exclusively attributed to the presence of the pair of shock waves. The anisotropy with the adiabatic cooling is negative. The particles decelerate faster at smaller radial distances, where the adiabatic cooling effect is stronger. As a result, more particles in the same energy range come from larger radial distances, and the anisotropy becomes negative.

At 4.5 AU (Panel (b6–7) in Figure 5), for the case without adiabatic cooling, we note that the proton distribution at 80 hours is not completely consistent with the profile of magnetic field magnitude. The intensity peak is on the IMF lines with $\varphi_{fp} \approx 263°$, while the magnetic field magnitude peak is on the IMF lines with $\varphi_{fp} \approx 247°$. Moreover, a new peak appears on the IMF lines with $\varphi_{fp} \approx 322°$. We infer that it attributes to the focusing length since the same seed particle population and radial mean free path is assumed on each IMF line. Smaller or negative focusing lengths could prevent particles from spreading to a larger radial distance (the pattern of L_B^{-1} is shown in the left panel of Figure 2). More particles remain and the intensity is greater on the IMF lines with a smaller focusing length after 80 hours. For the case with adiabatic cooling (the solid line), the profile remains a similar pattern but the longitudinal variation range is much larger. The anisotropy drops in the compressed region. On the one hand, the negative focusing length may reflect the particle backward. On the other hand, particles can be accelerated in the compressed region and move back.

In general, the particle intensity is influenced by the density of the magnetic field lines, the focusing effect, and the adiabatic effect. The focusing effect can change the shape of the distribution of particle intensity with longitude, and the adiabatic effect can increase the fluctuation of particle intensity with longitude.

3.1.2 The spectra variation

Figure 6 shows the spectra index at 1 AU varying with the foot point longitude. The spectral indices are obtained from a power-law fit to 1–10 MeV protons. The lines with different colors represent the results at different times. The solid and dashed lines represent the results with and without the adiabatic cooling effect. In the absence of adiabatic cooling effects, the spectral index increases with time in the IMF lines across the forward or reverse compression region, while it decreases with time in the IMF lines near the SI. This is because the negative focusing length

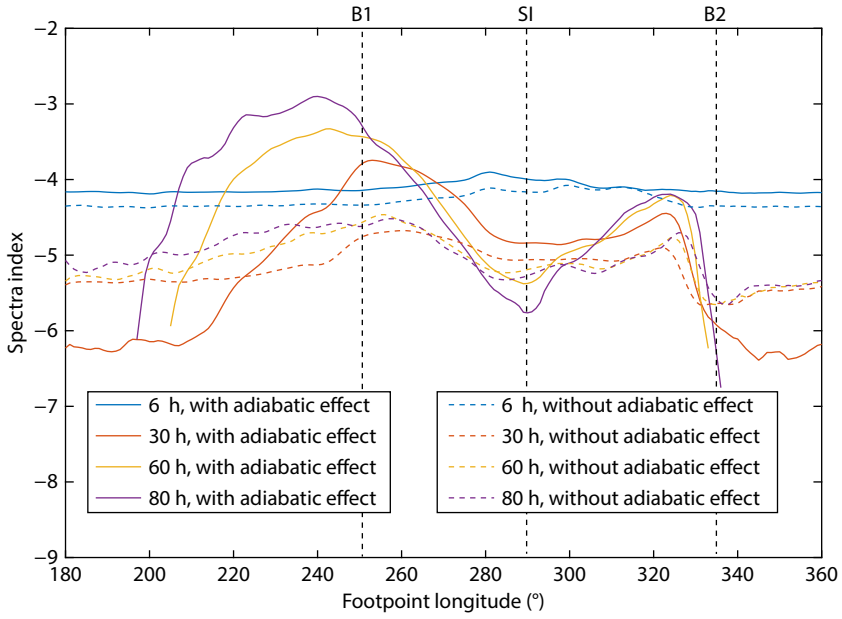

Figure 6. The spectra indices along the longitude evolving with time at 1 AU. The solid and dotted lines represent the results with and without adiabatic effect, respectively.

in the compressed region preserves more particles with higher energies at small radial distances. Due to the long focusing length near SI, the higher energy particles are transported faster to large radial distances, and few returned during this period.

In the presence of adiabatic cooling effects, the pattern of the evolution of the index with time is similar, except that the index varies more with longitude. In IMF lines similar to the Parker field, the index value is default due to the vanishing of higher energy particles. The adiabatic cooling effect in the Parker field leads to a decrease in particle energy, so that after 60 hours there are no more particles in the higher energy bands. The larger variation is mainly due to the compression acceleration effect on the higher energy particles. Figure 7 shows the time profile for particles at 1 AU with different energies along the magnetic field line with ϕ_{fp} = 200° and ϕ_{fp} = 220°. The low energy protons decay at a similar rate, while the high energy protons decay at a different rate. This may be because the ϕ_{fp} = 220° magnetic field line passes through the compression region at 4–5 AU (see Figure 2), while the ϕ_{fp} = 200° magnetic field line does not. On the ϕ_{fp} = 220° magnetic field line, the higher energy particles (7 MeV) accelerate in the compression region and return to 1 AU. Therefore, the intensity of the higher energy particles (the red dashed line) decreases more slowly than those along the ϕ_{fp} = 200° magnetic field line (the blue dashed line). The lower energy particles have not yet traveled that far, or the accelerated particles have not yet returned. So the lower energy particles are decaying at similar rates along the two magnetic field lines (the solid lines). This makes the spectral index different.

In order to clarify the acceleration effect of the background structure on the particles, Figure 8 demonstrates the energy change of particles along different IMF lines. We injected pseudoparticles with a certain initial energy (E_0) from the inner boundary at time t = 0. The initial energy (E_0), the energy at 80 hours (E), and the intensity of particles at 1 AU are recorded. We then plot the intensity in the E/E_0–E_0 coordinate. The x-axis is the energy injected (E_0). The y-axis is the ratio of the particle energy at 1 AU after 80 hours to its injected energy (E/E_0). The color represents the intensity logarithmic scale (the values are marked on the lines). The dashed black line shows the reference value of 1. The area above the dotted curve is out of our statistical range (The energy cut-off of our results is 10 MeV). Panel (a) shows the particle energy change on the IMF line in the approximate Parker field (φ_{fp} ≈ 200°). The particle energy at 80 hours is less than the injected energy due to the adiabatic cooling effect. Panel (b) shows particles on the IMF lines across the reverse compressed region (φ_{fp} ≈ 240°). The particle energy can be accelerated up to twice the injected energy. Panel (c) shows the conditions on the IMF lines across the forward compression region (φ_{fp} ≈ 315°). The particle energy can be accelerated above the injected energy (above the dashed line in the panel). The energy location at the peak value of intensity at 80 hours is about 70% of the injected energy. Our results are consistent with the former observations (Richardson, 2004) and simulations (Fisk and Lee, 1980; Wijsen et al., 2019a) that the particles at 1 AU can be accelerated to higher energy by the reverse shock than the forward one.

We can infer that the index pattern can be formed by focusing effects, because the negative focusing length in the compressed region preserves more energetic particles. The adiabatic effects can amplify the variation by accelerating or decelerating particles.

3.2 CIR Effect on SEP Variation with Radial Distance

3.2.1 The peak intensity of the energetic particles

Figure 9 shows the peak intensity varying along the heliocentric radius in different longitudes at the solar equator. The particles are injected at ±15° in latitude at inner boundary to make sure the particles at the solar equator are well connected to the uniform source. The empirical function $I_{max} = kR^{-\alpha}$ has often been used to describe the peak intensity I_{max} which varies with the radius of the heliosphere. As shown in Figure 9, with the effect of the compression regions, the peak intensity can increase by more than an order of magnitude compared to what the empirical power-law function would expect. Since the peak intensity may not follow a single power law at larger radius, we fit the radial distribution of

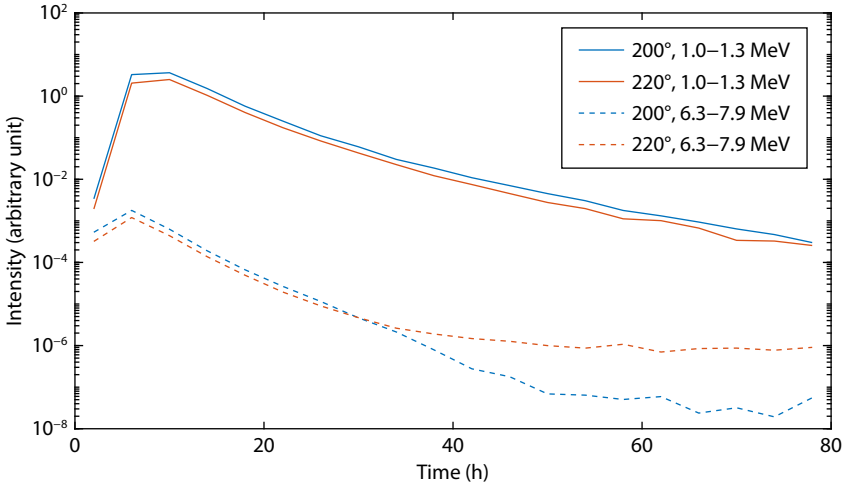

Figure 7. The time profile for particles at 1 AU with different energies along different magnetic field lines. The blue lines show profiles at ϕ_{fp} = 200° and the red lines show ϕ_{fp} = 220°. The solid lines show profiles for 1.0–1.3 MeV particles and the dashed lines for 6.3–7.9 MeV particles.

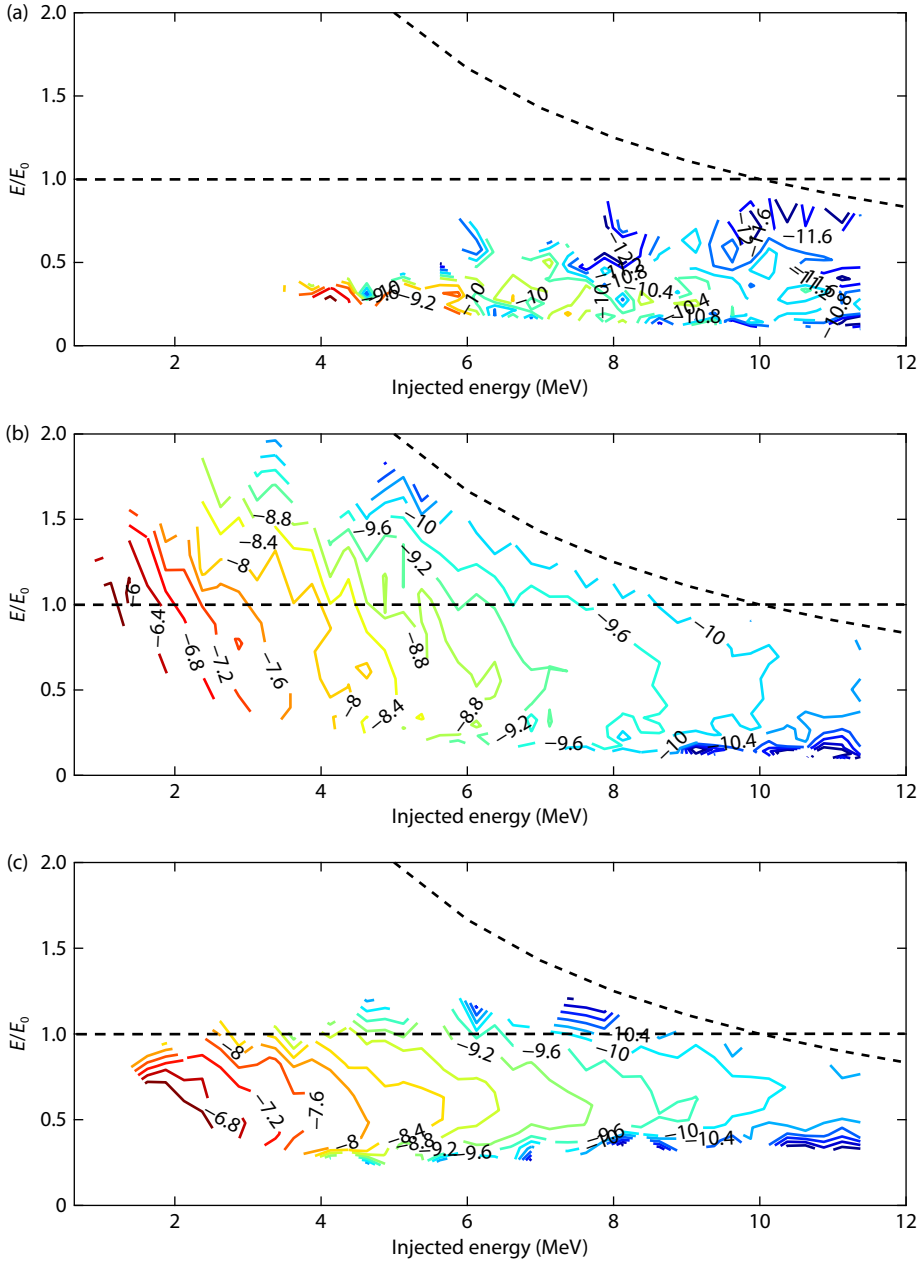

Figure 8. The energy change in the approximate Parker field (a), the reverse (b) and the forward (c) compression region. The *x*-axis represents the injected energy (E_0). The *y*-axis represents the ratio of the energy at 1 AU at 80 hours to the injected energy (E/E_0). The color represents the intensity logarithmic scale (the values are marked on the lines). The area above the black dotted curves is out of our statistical range. The reference value of 1 is shown with the black dashed lines.

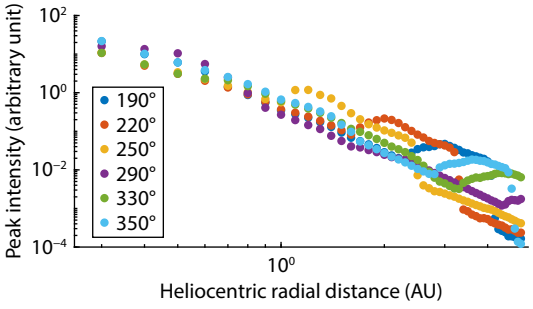

Figure 9. The peak intensity I_{max} of 1–10 MeV protons varying with radial distance R in different longitudes at the solar equator.

the peak intensity with the empirical function within 1 AU. To test whether this power-law empirical function is applicable in the CIR background structure, we then extrapolated the intensity with the empirical function using the obtained fitting value of α and the simulated intensity at 1 AU. The relative deviation $(I_{ext} - I_{sim})/I_{sim}$ between the extrapolated result I_{ext} and the simulation result I_{sim} is calculated. If the relative deviation of any point along the magnetic field line exceeds 60%, it is assumed that the power-law dependence does not apply well at that longitude.

Figure 10 shows the value of α fitted in 0.3–1.0 AU (black circles) varying with longitude, superimposed on the solar radial wind speed at 1 AU (the blue dashed line). The longitude for which the

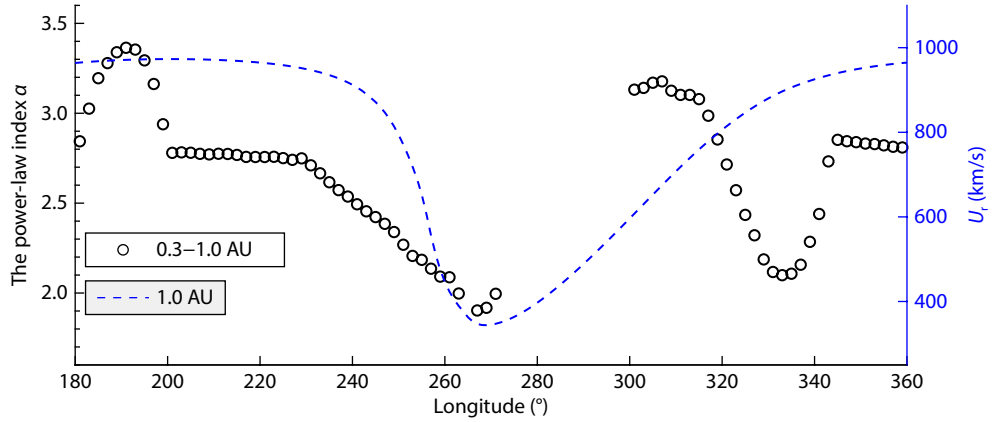

Figure 10. The black circles are the value of α varying with the longitude in the radial distance range of 0.3–1.0 AU. The longitudes for which the empirical function does not apply well are eliminated.

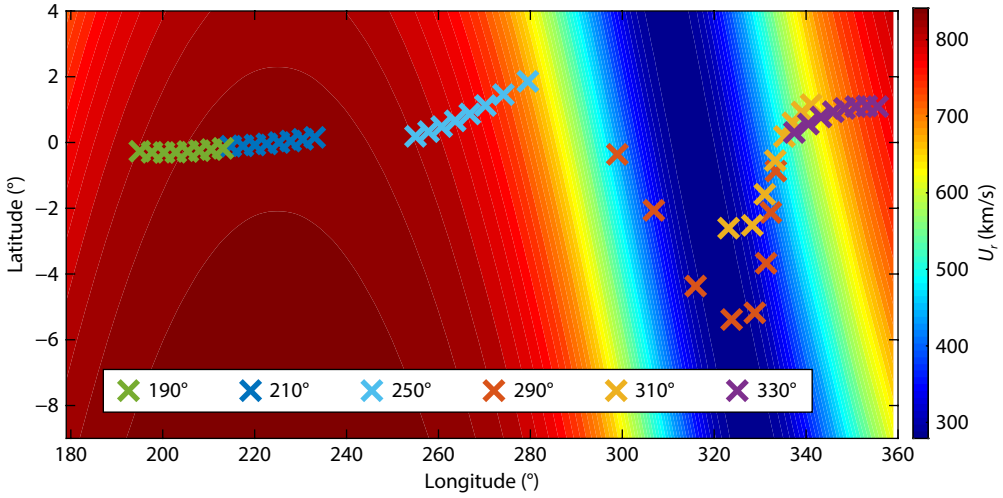

Figure 11. The footpoints of magnetic field lines passing through points along the heliocentric radius from 0.3 to 1.0 AU (at 0.1 AU intervals) at different longitudes, superimposed on the radial solar wind speed at the inner boundary (0.1 AU).

empirical function does not fit well are eliminated. Most of the longitude could be described by a power law in 0.3–1.0 AU, except for the region with the longitude of $270° < \phi < 300°$. The value of α ranges from 1.9 to 3.4 at 0.3–1.0 AU. To explain the variation of α with longitude, the footpoints of different longitudes superimposed on the radial solar wind speed at the inner boundary (0.1 AU) are shown in Figure 11. The crosses of the same color indicate the footpoints that are well connected to the points along the heliocentric radius from 0.3 to 1.0 AU (at 0.1 AU intervals) at the same longitude. The footpoint connected to a smaller radial distance has a smaller longitude. The blue crosses indicate the footpoints of longitude 210°. The solar wind speed at the footpoints is nearly the same at different radial distances. The value of α is about 2.8 at longitude 210°. The solar wind speed at the footpoints increases with radius at longitude 190° and 310°. Particles at larger radial distances are more affected by adiabatic cooling and thus have lower intensity at larger radial distances. Therefore, the value of α is larger at longitude 190° and 310°. Conversely, the solar wind speed at the footpoints decreases with radius at longitude 250°, and the value of α is smaller. In longitude 330° is a rarefaction region where the particles are less modulated by adiabatic cooling (Desai et al., 2020; Schwadron et al., 2021). Therefore the dependence of the intensity on the radius is smaller, and the value of α is smaller. The red crosses show the footpoints of the longitude 290°. As the radial distance increases, the solar wind speed at the footpoint decreases and then increases. The empirical power-law formula may not be applicable due to the non-monotonic variation of the solar wind speed with radius.

The experienced value of the index α varies in different observations. Verkhoglyadova et al. (2012) considered the effect of a traveling shock and perpendicular diffusion and found that the indices depend on the seed particle composition, the particle energy, the shock obliquity, and the interplanetary turbulence level. He HQ and Wan W (2017) simulated the particle transport in a Parker field and the index α is about 1.7 on the IMF lines directly connected to the particle resources. They pointed out that the value of the index α primarily depends on the magnetic connection status of the observers. Our result shows a variation from $R^{-3.4}$ to $R^{-1.9}$ within 1 AU for 1–10 MeV protons (without local enhancement). According to our results, we provide another explanation for the difference of α in observations. The index α may have a large range due to the structure of the solar wind, such as the

CIRs. The empirical power-law formula may not be applicable where the solar wind speed decreases to slow solar wind. The value of α decreases in the rarefaction region and in the region where the solar wind speed increases.

In addition, we investigated how α varies with particle energy. Figure 12 shows the index α varying with particle energy at different longitude within 1 AU. As shown in the figure, the index α decreases with energy in the range of 1–10 MeV. This makes sense because particles with higher energy move faster, and the intensity peaks are less dependent on the heliocentric radial distance. The index α becomes less dependent on particle energy in the larger energy channel. The results of He HQ et al. (2017) also suggest a weak energy dependence for high energy protons (higher than 10 MeV). The energy dependence is stronger in the lower energy channel (less than 3 MeV). Zhao LL et al. (2016) found a significant modulation of sub-MeV/nucleon particles. Our results are consistent with theirs.

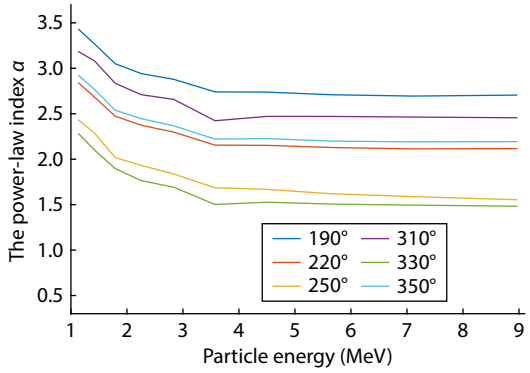

Figure 12. The value of index α varying with particle energy at different longitudes within 1 AU.

3.2.2 The spectra variation

Figure 13 shows the index of the fluence spectra varying with footpoint longitude at different radial distances. The fluence spectra are integrated for 80 hours after particle injection. There is no break in the spectra of 1–10 MeV protons. In the approximate Parker field, the spectral index varies from −4.6 to −3.7 as the radial distance increases from 0.5 AU to 3.0 AU. Fu S et al. (2022) reported a SEP event in which the fluence spectral index for

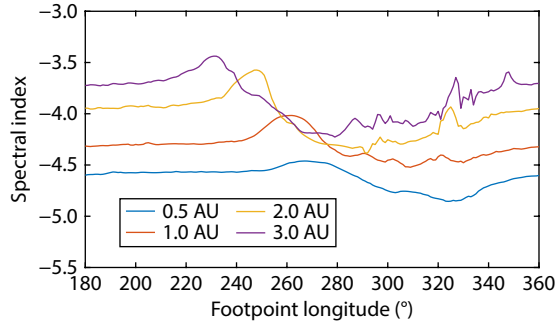

Figure 13. The proton (1–10 MeV) fluence spectral indices varying with footpoint longitude at different radial distances. The spectra are integrated over 80 hours after particle injection.

protons (a few MeV) is ~1.34 at the near-Earth spacecraft and ~0.67 at TW-1 (TianWen-1) (~1.39 AU). Our results in the approximate Parker field also show harder spectra at larger radial distances. In the CIR, however, the indices show a different variation with radial distance, even though the mean free path is set to the same value as in the approximate Parker field. Allen et al. (2021) analyzed the energetic proton observed in the same CIR and found that the indices at STA (~1 AU) and PSP (~0.5 AU) in the high-speed stream are approximately the same. Many observations (Joyce et al., 2021; Desai et al., 2020) indicate that the modulation is much weaker than what is predicted by existing models (Fisk and Lee, 1980; Zhao et al., 2016). Desai et al. (2020) believe that the existing models overestimate energy losses due to adiabatic deceleration. Schwadron et al. (2021) found that the sub-Parker magnetic field configuration helps explain the weak modulation. Although the seed populations in our simulations may be different from those in the observations, our results show that the spectral indices could be similar at different radial distances due to the CIR structure. As is shown in Figure 13, the indices are similar from 1.0 AU to 3.0 AU in the region with $\varphi_{fp} \approx 270°$. On the one hand, the adiabatic cooling effect is smaller in the region affected by the CIR (see the left panel in Figure 2). On the other hand, the compression region may accelerate the particles during propagation, compensating for the energy loss due to adiabatic deceleration. Therefore, it is necessary to take into account the large-scale background structure when studying the propagation of solar energetic particles.

4. Summary and Conclusions

CIRs generally have a substantial north-south tilt during the solar minimum. To investigate how this large-scale structure modulates the interplanetary transport of SEPs, we simulated a 3D tilted dipole CIR with the MHD model and coupled it to the SEP transport model. We describe the SEP transport by solving the FTE with a forward stochastic differential method.

We find that the solar wind near the SI is reflected not only to the east–west but also to the north–south direction. The field lines are compressed by the velocity component normal to the SI and stretched by the velocity component along the SI. For convenience, we extract the physical quantities along each magnetic field line.

On the one hand, the structures of the large-scale background play a role in the longitudinal variation of energetic particles. The large-scale background structure may be one of the reasons for the rippled peak intensity distribution observed at 1 AU (Klassen et al., 2016). The negative focusing length near the compression regions can modulate the intensity and form new longitudinal intensity peaks. It can also make the spectrum harder near the compression regions. The adiabatic effect can accelerate particles to higher energies in the compression regions. It can make the variation of intensity and spectrum index along the longitude larger.

On the other hand, the particle variation with heliocentric radial distance is also largely modulated by the interplanetary structure. The $-\alpha$ in the empirical function form $I_{\max} = kR^{-\alpha}$, which describes the peak intensity $I_{\max}$ varying with heliocentric radial distance,

varies largely in the observations. We found that, the peak intensities are well fitted by this empirical function at 0.3–1.0 AU, except in the region where the solar wind speed decreases until the minimum. The value of α is from 1.9 to 3.4 at 0.3–1.0 AU. The structure of the solar wind can also be used to explain the difference of α in observations according to our simulation. We suggest that the variation of the solar wind speed should be considered when estimating the radial dependence of the SEP peak intensities. Our results also suggest that, the radial variation of spectral indices may be different due to the CIR structure.

In this study, we only assume a simple model for the background field. Realistic interplanetary structures are much more complex, and particle distributions are correspondingly more complex. Therefore, it is important to model and predict background information more accurately and to take them into account in predicting SEP events.

Acknowledgement

This work is jointly supported by the National Natural Science Foundation of China (42330210 and 41974202), the National Key R&D Program of China (grant Nos. 2022YFF0503800 and 2021YFA0718600), the Strategic Priority Research Program of the Chinese Academy of Sciences (grant No. XDB 41000000), and the Specialized Research Fund for State Key Laboratories. We are grateful for discussions with Dr. Lulu Zhao and Dr. Wenwen Wei.

Supplementary Materials

Appendix A Verification of Our Method

We have verified our method by comparing our results with other studies. For example, Figure A1 shows our results setting the same condition with Panel (C) and (D) of Fig. 3 in Wijsen et al. (2019b). Figure A2 shows our results setting the same condition with Panel (1a) and (1b) of Fig. 2 in Wijsen et al. (2019a). Our results are consistent with theirs.

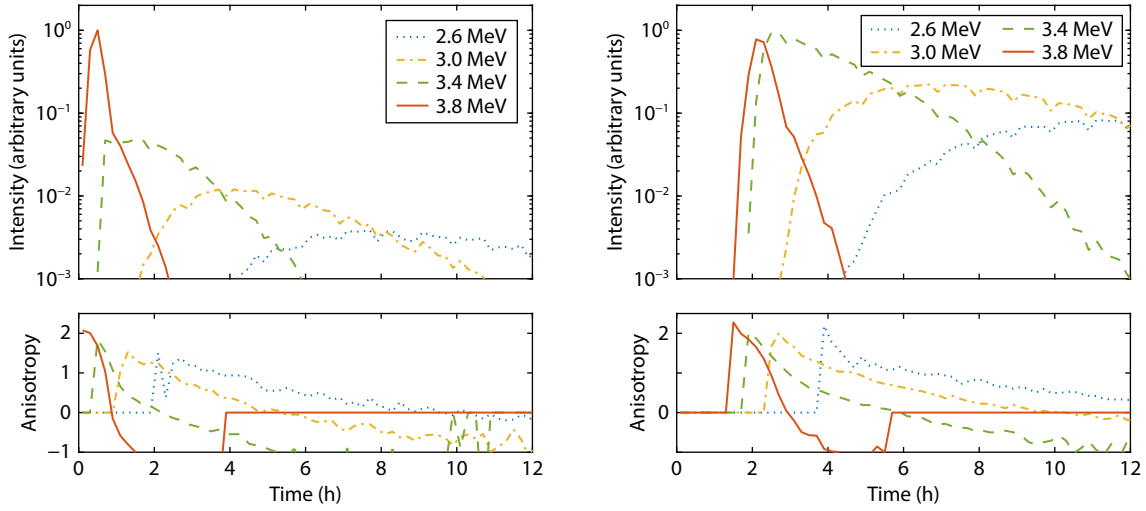

Figure A1. Our results setting the same condition with Panel (C) and (D) of Fig. 3 in Wijsen et al. (2019b). Intensity and anisotropy time profiles for different energy channels of protons injected with an initial energy of 4 MeV. The IMF is set as a Parker field with U_r = 700 km/s. The cross-field diffusion is ignored. The left and right columns show the results obvserved at 0.3 AU and 1.0 AU, respectively.

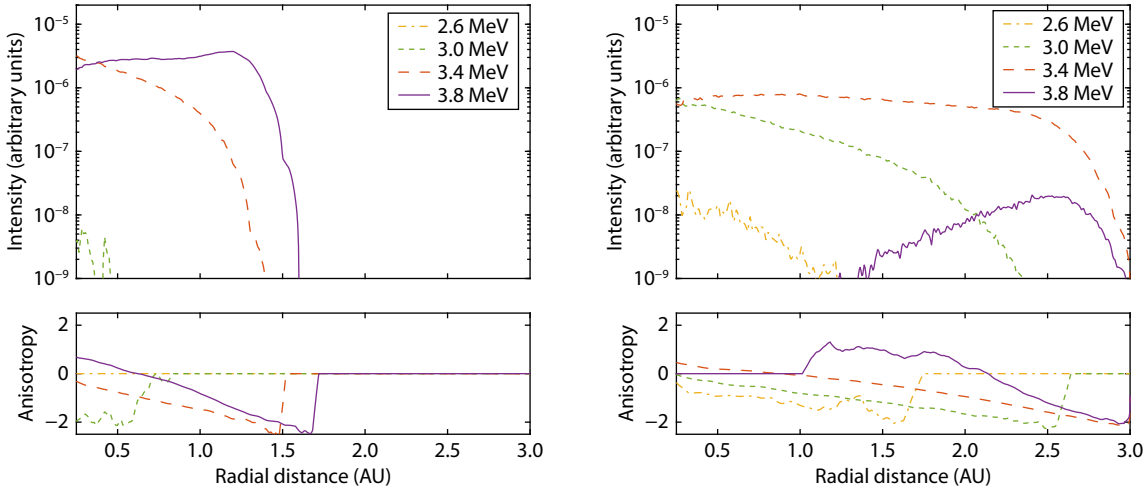

Figure A2. Our results setting the same condition with Panel (1a) and (1b) of Fig. 2 in Wijsen et al. (2019a). The particle intensities and anisotropies for different energy channels along a selected magnetic field line. The background is set as a Parker field with U_r = 330 km/s. The left and right columns are the results at 4 hours and 12.5 hours after particle injection, respectively.

References

Allen, R. C., Ho, G. C., Mason, G. M., Li, G., Jian, L. K., Vines, S. K., Schwadron, N. A., Joyce, C. J., Bale, S. D., … Wiedenbeck, M. (2021). Radial evolution of a CIR: Observations from a nearly radially aligned event between parker solar probe and STEREO-A. *Geophys. Res. Lett.*, *48*(3), e2020GL091376. https://doi.org/10.1029/2020gl091376

Altschuler, M. D., and Newkirk, G. Jr. (1969). Magnetic fields and the structure of the solar corona. *Solar Phys.*, *9*(1), 131–149. https://doi.org/10.1007/BF00145734

Arge, C. N., Odstrcil, D., Pizzo, V. J., and Mayer, L. R. (2003). Improved method for specifying solar wind speed near the sun. *AIP Conf. Proc.*, *679*(1), 190–193, https://doi.org/10.1063/1.1618574

Bobik, P., Boschini, M. J., Della, S. Torre, D., Gervasi, M., Grandi, D., La Vacca, G., Pensotti, S., Putis, M., … Zannoni, M. (2016). On the forward-backward-in-time approach for monte carlo solution of parker's transport equation: One-dimensional case. *J. Geophys. Res.: Space Phys.*, *121*(5), 3920–3930. https://doi.org/10.1002/2015ja022237

Desai, M., and Giacalone, J. (2016). Large gradual solar energetic particle events. *Living Reviews in Solar Physics*, *13*(1), https://doi.org/10.1007/s41116-016-0002-5

Desai, M. I., Mitchell, D. G., Szalay, J. R., Roelof, E. C., Giacalone, J., Hill, M. E., McComas, D. J., Christian, E. R., Schwadron, N. A., … Kasper, J. C. (2020). Properties of suprathermal-through-energetic he ions associated with stream interaction regions observed over the *parker solar* probe's first two orbits. *Astrophys. J. Suppl. Ser.*, *246*(2), 56. https://doi.org/10.3847/1538-4365/ab65ef

Dröge, W., Kartavykh, Y. Y., Klecker, B., and Kovaltsov, G. A. (2010). Anisotropic three-dimensional focused transport of solar energetic particles in the inner heliosphere. *Astrophys. J.*, *709*(2), 912–919. https://doi.org/10.1088/0004-637x/709/2/912

Feng, X. S., Wu, S. T., Wei, F. S., and Fan, Q. L. (2003). A class of TVD type combined numerical scheme for MHD equations with a survey about numerical methods in solar wind simulations. *Space Sci. Rev.*, *107*(1-2), 43–53. https://doi.org/10.1023/A:1025547016708

Feng, X. S., Yang, L. P., Xiang, C. Q., Wu, S. T., Zhou, Y. F., and Zhong, D. K. (2010). Three-dimensional solar *wind* modeling from the sun to Earth by a SIP-CESE MHD model with a six-component grid. *Astrophys. J.*, *723*(1), 300–319. https://doi.org/10.1088/0004-637x/723/1/300

Fisk, L. A., and Lee, M. A. (1980). Shock acceleration of energetic particles in corotating interaction regions in the solar wind. *Astrophys. J.*, *237*, 620–626. https://doi.org/10.1086/157907

Fu, S., Ding, Z. Y., Zhang, Y. J., Zhang, X. P., Li, C. H., Li, G., Tang, S. W., Zhang, H. Y., Xu, Y., … Xie, L. H. (2022). First report of a solar energetic particle event observed by China's Tianwen-1 mission in transit to mars. *Astrophys. J. Lett.*, *934*(1), L15. https://doi.org/10.3847/2041-8213/ac80f5

He, H. Q., and Wan, W. (2015). Numerical study of the longitudinally asymmetric distribution of solar energetic particles in the heliosphere. *Astrophys. J. Suppl. Ser.*, *218*(2), 17. https://doi.org/10.1088/0067-0049/218/2/17

He, H. Q., and Wan, W. (2017). On the east-west longitudinally asymmetric distribution of solar proton events. *Mon. Not. Roy. Astron. Soc.*, *464*(1), 85–93. https://doi.org/10.1093/mnras/stw2255

He, H. Q., Zhou, G., and Wan, W. (2017). Propagation of solar energetic particles in three-dimensional interplanetary magnetic fields: radial dependence of peak intensities. *Astrophys. J.*, *842*(2), 71. https://doi.org/10.3847/1538-4357/aa7574

Isenberg, P. A. (1997). A hemispherical model of anisotropic interstellar pickup ions. *J. Geophys. Res.: Space Phys.*, *102*(A3), 4719–4724. https://doi.org/10.1029/96ja03671

Jian, L., Russell, C. T., Luhmann, J. G., and Skoug, R. M. (2006). Properties of stream interactions at one au during 1995-2004. *Solar Phys.*, *239*(1-2), 337-392. https://doi.org/10.1007/s11207-006-0132-3

Joyce, C. J., McComas, D. J., Schwadron, N. A., Christian, E. R., Wiedenbeck, M. E., McNutt, R. L., Cohen, C. M. S., Leske, R. A., Mewaldt, R. A., … Kasper, J. C. (2021). Time evolution of stream interaction region energetic particle spectra in the inner heliosphere. *Astron. Astrophys.*, *650*, L5. https://doi.org/10.1051/0004-6361/202039330

Kallenrode, M. B. (1997). A statistical study of the spatial evolution of shock acceleration efficiency for 5 MEV protons and subsequent particle propagation. *J. Geophys. Res.: Space Phys.*, *102*(A10), 22335–22345. https://doi.org/10.1029/97ja02035

Klassen, A., Dresing, N., Gómez-Herrero, R., Heber, B., and Müller-Mellin, R. (2016). Unexpected spatial intensity distributions and onset timing of solar electron events observed by closely spaced stereo spacecraft. *Astron. Astrophys.*, *593*, A31. https://doi.org/10.1051/0004-6361/201628734

Kocharov, L., Kovaltsov, G. A., Torsti, J., Anttila, A., and Sahla, T. (2003). Modeling the propagation of solar energetic particles in corotating compression regions of solar wind. *J. Geophys. Res.: Space Phys.*, *108*(A11), 1404. https://doi.org/10.1029/2003ja009928

Kocharov, L., Pizzo, V. J., Zwickl, R. D., and Valtonen, E. (2008). A new approach to interplanetary transport of solar energetic particles in impulsive events. *Astrophys. J.*, *680*(1), L69–L72. https://doi.org/10.1086/589829

Kocharov, L., Pizzo, V. J., Odstrcil, D., and Zwickl, R. D. (2009). A unified model of solar energetic particle transport in structured solar wind. *J. Geophys. Res.: Space Phys.*, *114*(A5), A05102. https://doi.org/10.1029/2008ja013837

Kopp, A., Büsching, I., Strauss, R. D., and Potgieter, M. S. (2012). A stochastic differential equation code for multidimensional fokker-planck type problems. *Comput. Phys. Commun.*, *183*(3), 530–542. https://doi.org/10.1016/j.cpc.2011.11.014

Kozarev, K., Schwadron, N. A., Dayeh, M. A., Townsend, L. W., Desai, M. I., and PourArsalan, M. (2010). Modeling the 2003 Halloween events with EMMREM: energetic particles, radial gradients, and coupling to MHD. *Space Wea.*, *8*(11), S00E08. https://doi.org/10.1029/2009sw000550

Lario, D., Kallenrode, M. B., Decker, R. B., Roelof, E. C., Krimigis, S. M., Aran, A., and Sanahuja, B. (2006). Radial and longitudinal dependence of solar 4-13 MeV and 27-37 MeV proton peak intensities and fluences: *Helios* and *IMP 8* observations. *Astrophys. J.*, *653*(2), 1531–1544. https://doi.org/10.1086/508982

Lario, D., Aran, A., Agueda, N., and Sanahuja, B. (2007). Radial dependence of proton peak intensities and fluences in SEP events: Influence of the energetic particle transport parameters. *Adv. Space Res.*, *40*(3), 289–294. https://doi.org/10.1016/j.asr.2007.01.057

Lario, D., Aran, A., Gómez-Herrero, R., Dresing, N., Heber, B., Ho, G. C., Decker, R. B., and Roelof, E. C. (2013). Longitudinal and radial dependence of solar energetic particle peak intensities: Stereo, ace, *soho, goes*, and messenger observations. *Astrophys. J.*, *767*(1), 41. https://doi.org/10.1088/0004-637x/767/1/41

le Roux, J. A., and Webb, G. M. (2009). Time-dependent acceleration of interstellar pickup ions at the heliospheric termination shock using a focused transport approach. *Astrophysical J.*, *693*(1), 534–551. https://doi.org/10.1088/0004-637x/693/1/534

Leske, R. A., Christian, E. R., Cohen, C. M. S., Cummings, A. C., Davis, A. J., Desai, M. I., Giacalone, J., Hill, M. E., Joyce, C. J., … and Poduval, B. (2020). Observations of the 2019 april 4 solar energetic particle event at the parker solar probe. *Astrophys. J. Suppl. Ser.*, *246*(2), 35. https://doi.org/10.3847/1538-4365/ab5712

Neugebauer, W., and Snyder, M. (1962). The mission of mariner II: Preliminary observations profile of events. *Science, 138*(3545), 1095. https://doi.org/10.1126/science.138.3545.1095.

Reames, D. V. (1999). Particle acceleration at the Sun and in the heliosphere. *Space Science Reviews*, *90*(3-4), 413–491 https://doi.org/10.1023/A:1005105831781

Reid, G. C. (1964). A diffusive model for the initial phase of a solar proton event. *J. Geophys. Res.: Space Phys.*, *69*(13), 2659–2667. https://doi.org/10.1029/JZ069i013p02659

Richardson, I. G. (2004). Energetic particles and corotating interaction regions in the solar wind. *Space Sci. Rev.*, *111*(3-4), 267–376. https://doi.org/10.1023/B:SPAC.0000032689.52830.3e

Richardson, I. G., von Rosenvinge, T. T., Cane, H. V., Christian, E. R., Cohen, C. M. S., Labrador, A. W., Leske, R. A., Mewaldt, R. A., Wiedenbeck, M. E., and Stone, E. C. (2014). > 25 MeV proton events observed by the high energy telescopes on the STEREO A and B spacecraft and/or at Earth during the

first ~ seven years of the STEREO mission. *Solar Phys.*, *289*(8), 3059–3107. https://doi.org/10.1007/s11207-014-0524-8

Schatten, K. H., Wilcox, J. M., and Ness, N. F. (1969). A model of interplanetary and coronal magnetic fields. *Solar Phys.*, *6*(3), 442–455. https://doi.org/10.1007/Bf00146478

Schwadron, N. A., Joyce, C. J., Aly, A., Cohen, C. M. S., Desai, M. I., McComas, D. J., Niehof, J. T., E. Möbius, Lee, M., … Wiedenbeck, M. E. (2021). A new view of energetic particles from stream interaction regions observed by parker solar probe. *Astron. Astrophys.*, *650*, A24. https://doi.org/10.1051/0004-6361/202039352

Shen, F., Feng, X. S., Wu, S. T., and Xiang, C. Q. (2007). Three-dimensional MHD simulation of CMES in three-dimensional background solar wind with the self-consistent structure on the source surface as input: numerical simulation of the January 1997 sun-earth connection event. *J. Geophys. Res.: Space Phys.*, *112*(A6), A06109. https://doi.org/10.1029/2006ja012164

Shen, F., Feng, X. S., and Song, W. B. (2009). An asynchronous and parallel time-marching method: application to three-dimensional MHD simulation of solar wind. *Sci. China Ser. E: Technol. Sci.*, *52*(10), 2895–2902. https://doi.org/10.1007/s11431-009-0291-1

Shen, F., Yang, Z. C., Zhang, J., Wei, W. W., and Feng, X. S. (2018). Three-dimensional MHD simulation of solar wind using a new boundary treatment: Comparison with in situ data at earth. *Astrophys. J.*, *866*(1), 18. https://doi.org/10.3847/1538-4357/aad806

Skilling, J. (1971). Cosmic rays in the galaxy: Convection or diffusion?. *Astrophys. J.*, *170*, 265. https://doi.org/10.1086/151210

Smith, E. J., and Wolfe, J. H. (1979). Fields and plasmas in the outer solar system. *Space Science Reviews*, *23*(2), 217–252.

Strauss, R. D., and Fichtner, H. (2015). On aspects pertaining to the perpendicular diffusion of solar energetic particles. *Astrophys. J.*, *801*(1), 29. https://doi.org/10.1088/0004-637x/801/1/29

Strauss, R. D. T., and Effenberger, F. (2017). A hitch-hiker's guide to stochastic differential equations. *Space Sci. Rev.*, *212*(1-2), 151–192. https://doi.org/10.1007/s11214-017-0351-y

Totten, T. L., Freeman, J. W., and Arya, S. (1995). An empirical determination of the polytropic index for the free-streaming solar wind using Helios 1 data. *J. Geophys. Res.: Space Phys.*, *100*(A1), 13–17. https://doi.org/10.1029/94JA02420

Tsubouchi, K. (2014). Particle acceleration at corotating interaction regions in the heliosphere. *Astrophys. J.*, *795*(1), 47. https://doi.org/10.1088/0004-637x/795/1/47

Verkhoglyadova, O. P., Li, G., Ao, X., and Zank, G. P. (2012). Radial dependence of peak proton and iron ion fluxes in solar energetic particle events: application of the path code. *Astrophys. J.*, *757*(1), 75. https://doi.org/10.1088/0004-637x/757/1/75

Wei, W. W., Shen, F., Yang, Z. C., Zhao, L. L., Wang, Y., Zuo, P. B., and Zhang, J. (2019). Modeling solar energetic particle transport in 3D background solar wind: influences of the compression regions. *J. Atmos. Sol-Terr. Phys.*, *182*, 155–164. https://doi.org/10.1016/j.jastp.2018.11.012

Wijsen, N., Aran, A., Pomoell, J., and Poedts, S. (2019a). Interplanetary spread of solar energetic protons near a high-speed solar wind stream. *Astron. Astrophys.*, *624*, A47. https://doi.org/10.1051/0004-6361/201935139

Wijsen, N., Aran, A., Pomoell, J., and Poedts, S. (2019b). Modelling three-dimensional transport of solar energetic protons in a corotating interaction region generated with EUHFORIA. *Astron. Astrophys.*, *622*, A28. https://doi.org/10.1051/0004-6361/201833958

Zhang, M., Qin, G., and Rassoul, H. (2009). Propagation of solar energetic particles in three-dimensional interplanetary magnetic fields. *Astrophys. J.*, *692*(1), 109–132. https://doi.org/10.1088/0004-637x/692/1/109

Zhao, L. L., Li, G., Ebert, R. W., Dayeh, M. A., Desai, M. I., Mason, G. M., Wu, Z., and Chen, Y. (2016). Modeling transport of energetic particles in corotating interaction regions: a case study. *J. Geophys. Res.: Space Phys.*, *121*(1), 77–92. https://doi.org/10.1002/2015ja021762

Zhao, L. L., Zhang, M., and Lario, D. (2020). Modeling the transport processes of a pair of solar energetic particle events observed by parker solar probe near perihelion. *Astrophys. J.*, *898*(1), 16. https://doi.org/10.3847/1538-4357/ab97b3